Available online at www.sciencedirect.com
SCIENCE DIRECT
Journal of Computational Physics 214 (2006) 81–95
JOURNAL OF COMPUTATIONAL PHYSICS
www.elsevier.com/locate/jcp

Efficient calculation of current densities in the human body induced by arbitrarily shaped, low-frequency magnetic field sources

Andreas Barchanski [a,*], Markus Clemens [b], Herbert De Gersem [a], Thomas Weiland [a]

[a] *Technische Universität Darmstadt, Institut für Theorie Elektromagnetischer Felder, Fachbereich Elektrotechnik und Informationstechnik, Schlossgartenstrasse 8, D-64289 Darmstadt, Germany*

[b] *Helmut-Schmidt-Universität, Universität der Bundeswehr Hamburg, Professur für Theoretische Elektrotechnik und Numerische Feldberechnung, P.O. Box 700833, 22008 Hamburg, Germany*

Received 18 May 2005; received in revised form 10 August 2005; accepted 13 September 2005
Available online 11 November 2005

Abstract

In this paper, we extend the scalar-potential finite-difference (SPFD) approach in order to consider arbitrarily shaped time-harmonic field sources. The SPFD approach is commonly used to compute the currents induced by an externally applied magnetic field in regions with weak, heterogeneous conductivities such as, e.g., the human body. We present the extended scalar-potential finite-difference (Ex-SPFD) approach as a two step algorithm. In the first step, the excitation is computed by solving the magnetoquasistatic curl–curl equation on a coarse grid that is well adapted for the field sources. In the second step, the magnetic vector potential is prolongated onto a finer grid and a divergence correction inside the conductor is applied. Using the Maxwell-grid-equations (MGEs) of the finite integration technique, a geometric discretization scheme for Maxwell's equations, this new approach has been implemented in a parallel environment in order to account for the memory-demanding high-resolution anatomy models used for the calculation of induced currents inside the human body. We demonstrate the validity and the improved numerical performance of the new approach for a test case. Finally, an application example of a human exposed to a realistic electromagnetic field source is presented.

Keywords: Dosimetry; Human-body; ELF; Induced currents

1. Introduction

An increasing demand to understand and quantify the interaction of electromagnetic fields with biological tissue has arisen in public discussion throughout the past years, additionally fueled by recurring reports in the

* Corresponding author. Tel.: +49 6151 164783; fax: +49 6151 164611.
E-mail addresses: barchanski@temf.tu-darmstadt.de (A. Barchanski), markus.clemens@hsu-hh.de (M. Clemens), degersem@temf.tu-darmstadt.de (H. De Gersem), thomas.weiland@temf.tu-darmstadt.de (T. Weiland).
URLs: http://www.temf.de (A. Barchanski), http://www.hsu-hh.de/tet (M. Clemens).

0021-9991/$ - see front matter
doi:10.1016/j.jcp.2005.09.009

media. In this vast research area, it is necessary to consider epidemiological, biological and dosimetric studies in order to derive basic restriction guidelines and minimize the possibility of harmful effects.

The exposure of the human body to ambient low-frequency magnetic fields results in an induced current density distribution in the weak conductive biological tissue. Such fields can originate not only from strong currents like in welding processes and magnetodynamic energy converters but also from electrical power lines and domestic electrical devices. The induced current densities inside the body can result in an excitation of the biological system. Above 10 mA/m^2 visual phosphene inside the eye has been observed, and above 100 mA/m^2 a direct stimulation of the muscles and the nervous system can occur [1]. Therefore, the International Commission on non-ionizing radiation protection (ICNIRP) has proposed a basic restriction of 2 mA/m^2 for the general public [2] which was adapted by various governments throughout the world.

Since it is nearly impossible to measure electromagnetic quantities inside the human body in vivo, computational dosimetry is applied to estimate the electromagnetic field quantities inside the body. Various computational techniques have been introduced in order to tackle this problem. Due to the complicated structure of the human body, consisting of organs with varying dimensions and geometrically complicated shapes, all exhibiting different electrical properties, a very fine spatial resolution is needed to achieve as accurate results as possible. The state-of-the-art approach for the computation of electromagnetic fields inside the body is to solve Maxwell's equations numerically in high-resolution, anatomically realistic human body models.

The first calculations of current densities inside the human body, arising from low-frequency magnetic fields, that were based on (semi-)realistic voxel models used the impedance method and were performed by Gandhi in 1984 [3]. In this method, the voxels are differentiated into a three-dimensional network of impedances. Around the closed loop of each voxel-face the time-varying magnetic field induces a voltage which is used to calculate the induced current density. The coupled equations for the loop currents are merged into one system of equations that can be solved iteratively. Further details on the impedance method and their application to low-frequency electromagnetic fields inside the human body can be found in [4–6]. The scalar-potential finite-difference (SPFD) approach was introduced in 1996 by Stuchly and Dawson [7–9]. In this approach, the magnetic field sources are represented by a magnetic vector potential and the computational domain is discretized with the finite difference method. A more detailed description of the SPFD approach will be given in Section 3. A comparison of both techniques and their results can be found in [10] while a recent review of the computational methods and interaction mechanisms was published in [11].

The paper is organized as follows: In Section 2, a brief description of the used anatomy model and the used tissue parameters is given. Section 3 covers the mathematical framework of the discrete electromagnetic formulation. Beginning with an introduction to the finite integration technique (FIT), the electromagnetic curl–curl equation, the SPFD approach and the new extended scalar-potential finite-differences approach (Ex-SPFD) are presented. Section 4 presents numerical results for a test-case scenario and the validity of the presented approach together with performance results. Following the numerical results section, an application example of a human exposed to a low-frequency magnetic field due to a realistic source is presented. Finally, the paper ends with a summary.

2. Anatomy model and electromagnetic properties of biological tissue

In the early days of computational dosimetry, the human body was modeled by simple geometrical structures, like prolate spheroids or ellipsoids [12,13]. Such simple models can only crudely approximate the complex structure and the significant inhomogeneity of the human body. The next generation of human-body models used for electromagnetic field calculations were voxel based [14], but yet at very coarse resolutions. These voxel models were not directly derived from medical data, like it is state-of-the-art nowadays, but they still approximated the shape of the human body in a more exact way than simple spheroids. The vast progress in medical imaging during the 80's lead to the possibility of creating digital anatomy models based on real-word data. The *Visible Human Project* founded by the *United States National Library of Medicine* [15] formulated the goal of "building a digital image library of volumetric data representing a complete, normal adult male and female" in 1989. Using images from cryosectioning, digital images from computerized tomography and magnetic resonance imaging, a collection of cross-sectional images was established and made public in 1994. Nowadays very comfortable, free-of-charge interfaces to this database exist on the internet (e.g. [16]).

In this work the *HUGO* model, which has been constructed from the Visible Human Dataset, was used. The used model offers a variable resolution ranging from $8 \times 8 \times 8$ mm^3 to $1 \times 1 \times 1$ mm^3 for the edges of the voxels. Each voxel is assigned one tissue type, with a total of 31 various tissue types, see Table 1 for a listing of available tissues. In the finest resolution, the model consists of approximately 380 million voxels, representing a 38 years old, male person of 187 cm height and an approximate weight of 114 kg. Informations about models used by other groups for computational dosimetry can be found in [17–19].

With the anatomy model providing the geometrical structure, the electromagnetic properties of biological tissue are still needed in order to perform dosimetric simulations. The study of the electromagnetic properties of biological tissue have been of interest for over a century now, and is still an active area in actual research. The main challenge remains the measurement of the electromagnetic properties of isolated organs in vivo over a broad frequency range. Since the human body consist of non-magnetic materials, the permeability of the entire body can be set to the vacuum permeability. For the dielectric properties, Cole [20] proposed a formula for calculating the permittivity and conductivity in a wide frequency range. In 1996, Gabriel et al. published a large literature survey [21] combined with new measurements [22] and accompanied by a parameter extraction for the Cole–Cole equation [23]. This results became widely accepted by the scientific community and have been used for various dosimetric computations. The electric tissue properties used in this article have been calculated using the extended model proposed by Gabriel et al., and are summarized in Table 1.

Equipped with the high-resolution anatomy-model and the electric properties of tissue we are now ready to introduce the discrete electromagnetic theory and the algorithms used for the calculation of induced current densities in the following section.

Table 1
Available tissue types, corresponding electric conductivities and fractions of occurrence in the *HUGO* model (resolution: 1 mm^3)

Tissue type	Conductivity @ 50 Hz [S/m]	% of body
Marrow	0.0016	2.74
Fat tissue	0.0195	37.51
Bones	0.02	6.78
White substance	0.053	0.48
Grey substance	0.075	0.57
Skin	0.0002	1.88
Eye	1.5	0.01
Skeleton muscle	0.23	39.20
Blood	0.7	0.66
Neuronal fabric	0.027	0.15
Eye lens	0.32	0.00
Nevus opticus	0.027	0.14
Cartilages	0.17	0.36
Mucous membrane	0.00042	0.09
Lung	0.205	3.27
Intestine	0.52	1.17
Kidney	0.089	0.32
Liver	0.0367	1.69
Glands	0.52	0.12
Spleen	0.086	0.21
Stomach	0.521	0.15
Pancreas	0.521	0.08
Bladder	0.205	0.08
Gall bladder	0.9	0.02
Intestine contents	0.5	1.73
Ventricles right	0.0827	0.08
Ventricles left	0.0827	0.16
Forecourt right	0.0827	0.03
Forecourt left	0.0827	0.03
Blood venous	0.7	0.22
Blood arterial	0.7	0.06

3. Mathematical framework

In the beginning of this section, the FIT along with the commonly used notation is summarized, before presenting the algorithms for induced current computation. Because the Extended-SPFD formulation is based on the electromagnetic curl–curl equation for calculating the magnetic source field and the SPFD approach for estimating the induced currents inside the conductor, both schemes will be described, prior to introducing the Extended-SPFD formulation.

3.1. Finite integration technique

The FIT was first formulated by Weiland in 1977 [24] and has been developed further throughout the years by numerous contributors, resulting in a extensive library of discrete electromagnetic formulations. Only a very brief introduction will be given here, readers interested in further details of FIT are referred to [25–28].

The FIT is based on a geometrical discretization of the Maxwell equations in the integral form. Along with the constitutive material relations, the Maxwell equations are mapped onto an staggered, dual, orthogonal grid pair. Instead of field quantities defined at points, integral state variables assigned to all possible geometric primitives of the grid are used to formulate the problem. The electric voltage $\widehat{\mathbf{e}}$, the magnetic voltage $\widehat{\mathbf{h}}$, the electric flux $\widehat{\widehat{\mathbf{d}}}$, the electric current $\widehat{\widehat{\mathbf{j}}}$, and the magnetic flux $\widehat{\widehat{\mathbf{b}}}$, are defined by line and surface integrals of the elementary field values $\vec{E}$ (electric field intensity), $\vec{H}$ (magnetic field intensity), $\vec{D}$ (electric flux density), $\vec{J}$ (electric current density), and $\vec{B}$ (magnetic flux density). The continuous curl and divergence operators are expressed by the discrete operators $\mathbf{C}$ and $\widetilde{\mathbf{C}}$ for the curl, $\mathbf{S}$ and $\widetilde{\mathbf{S}}$ for the divergence on the primal and dual grid, respectively. The discrete equations arising in terms of these operators are often referred to as the Maxwell grid equations (MGEs). These equations are per construction exact for the used mesh pair.

The approximation in this discretization method appears when the integral voltage and flux state variables have to be coupled for actual field computations. The material matrices $\mathbf{M}_\mu$, $\mathbf{M}_\varepsilon$ and $\mathbf{M}_\kappa$ represent the discrete matrices of permeability μ, permittivity ε and conductivity κ, respectively. The material matrices can be constructed using various averaging techniques, that are beyond the scope of this article and can be found in [29–32]. In the case of computations presented here based on a voxel model, a straightforward averaging technique of the conductivity and permittivity over a dual facet $\widetilde{A}_n$ is applied.

The induced current calculations will be performed in the frequency domain, assuming that the system is in a steady state and no transient effects have to be considered. All field quantities are time-harmonic and can be transformed into the time domain by means of a Fourier transformation

$$f(t) = \Re\{\underline{f} \cdot \mathrm{e}^{\mathrm{i}\omega t}\}. \tag{1}$$

In the frequency domain the time derivative of a quantity can be expressed by an algebraic multiplication of the complex amplitude with the factor $\mathrm{i}\omega$.

3.2. Electromagnetic curl–curl equation

Starting with the Maxwell's curl equations in the frequency domain,

$$\nabla \times \underline{\vec{E}} = -\mathrm{i}\omega \underline{\vec{B}}, \tag{2}$$

$$\nabla \times \underline{\vec{H}} = \mathrm{i}\omega \underline{\vec{D}} + \underline{\vec{J}}, \tag{3}$$

either the magnetic or the electric field can be eliminated, leading to only one equation in terms of the non-eliminated field quantity. In the case of eliminating the magnetic component, this yields

$$\mathbf{curl}\,\mu^{-1}\mathbf{curl}\,\underline{\vec{E}} + \mathrm{i}\omega\kappa\underline{\vec{E}} - \omega^2\varepsilon\underline{\vec{E}} = -\mathrm{i}\omega\underline{\vec{J}}_S, \tag{4}$$

with the excitation current $\underline{\vec{J}}_S$. Using the FIT discretization the curl–curl equation reads

$$[\widetilde{\mathbf{C}}\mathbf{M}_\nu\mathbf{C} + \mathrm{i}\omega\mathbf{M}_\kappa - \omega^2\mathbf{M}_\varepsilon]\underline{\widehat{\mathbf{e}}} = -\mathrm{i}\omega\underline{\widehat{\widehat{\mathbf{j}}}}_s, \tag{5}$$

where $\mathbf{M}_\nu$ denotes the material matrix of the inverse permeability $\nu = \mu^{-1}$. Because the displacement current is explicitly considered, the curl–curl equation is valid in the whole frequency range, allowing the calculation of wave propagation phenomena as well as problems in the magneto-quasistatic case, where the displacement currents can be neglected [33]. But this generality also has its price: Simulating low-frequency fields with the curl–curl equation (ω near zero) the solution of the system lies near the static eigenmodes of the multiply trivial eigenvalue ($\omega = 0$) of the system matrix. In exact arithmetic this is not a problem, but when solving the system iteratively, the singular $\widetilde{\mathbf{C}}\mathbf{M}_\nu\mathbf{C}$ term numerically dominates the equation, leading to a slow convergence of the solution parts related to the eddy current losses that are governed by the $\mathrm{i}\omega\mathbf{M}_\kappa - \omega^2\,\mathbf{M}_\varepsilon$ term in the system matrix. This effect is even more pronounced for models with low conductivity values, which are the case for biological tissues. Therefore, Eq. (5) is augmented with a grad–div term, additionally enforcing the relation $\widetilde{\mathbf{S}}[\mathrm{i}\omega\mathbf{M}_\kappa - \omega^2\mathbf{M}_\varepsilon]\widehat{\underline{\mathbf{e}}} = 0$ inside the computational domain [34], which is inherently given by left application of the divergence operator on (5). A positive (semi-)definite norm matrix $\mathbf{M}_N$ ensures the correct units for the augmentation term and furthermore prevents a deterioration of the condition number. The augmented curl–curl formulation reads

$$[\widetilde{\mathbf{C}}\mathbf{M}_\nu\mathbf{C} + \mathbf{M}_\kappa\widetilde{\mathbf{S}}^{\mathrm{T}}\mathbf{M}_N\widetilde{\mathbf{S}}\mathbf{M}_\kappa + \mathrm{i}\omega\mathbf{M}_\kappa - \omega^2\mathbf{M}_\varepsilon]\widehat{\underline{\mathbf{e}}} = -\mathrm{i}\omega\widehat{\underline{\mathbf{j}}}_s \tag{6}$$

and will be used throughout the rest of this paper, omitting the word ''augmented'' when referred to it.

3.3. Scalar-potential finite-differences approach

The SPFD approach has been frequently used by Stuchly et al. [8,9] for the calculation of low-frequency induced currents in the human body. It is valid in the magnetoquasistatic case [7] when the eddy current losses are relatively small. Basically, it can be understood as an inhomogeneous stationary current field problem, without accounting for shielding effects of conductors present in the computational domain.

Starting with an additive decomposition of the potential into a rotational part, represented by the vector potential $\underline{\vec{A}}_0$, and an irrotational part represented by the gradient of a scalar potential $\nabla\underline{\phi}$, we obtain

$$\begin{aligned}\underline{\vec{E}} &= -\mathrm{i}\omega(\underline{\vec{A}}_0 + \nabla\underline{\phi})\\ \underline{\vec{B}}_0 &= \nabla\times\underline{\vec{A}}_0,\end{aligned} \tag{7}$$

and using the quasistatic continuity equation

$$\nabla\cdot\underline{\vec{J}} = \nabla\cdot(\kappa\vec{E}) = 0 \tag{8}$$

results in the SPFD equation

$$-\nabla\cdot(\kappa\nabla\underline{\phi}) = \nabla\cdot(\kappa\underline{\vec{A}}_0), \tag{9}$$

which has to be solved inside the conductor. This formulation discretized by the FIT reads

$$\widetilde{\mathbf{S}}\mathbf{M}_\kappa\widetilde{\mathbf{S}}^{\mathrm{T}}\underline{\phi} = \widetilde{\mathbf{S}}\mathbf{M}_\kappa\widehat{\underline{\mathbf{a}}}_0. \tag{10}$$

In order to calculate the induced currents inside the conductor, the magnetic vector potential $\underline{\vec{A}}_0$ has to be known inside the computational domain. This fact limits the field sources to ones that are known analytically or semi-analytically. Furthermore, it makes this approach only valid, when shielding effects of possibly present high-conductive materials can be neglected entirely. For that case this formulation is very efficient. The neglect of shielding effects is well justified in the case of the human body, where the conductivities are fairly low. On the other hand this disallows the presence of high conductive material, like metallic implants, in the computational domain.

3.4. Extended scalar-potential finite-differences approach

The Ex-SPFD approach combines the advantages of the both previously presented schemes into a two-step procedure. In the first step, the electromagnetic curl–curl equation (6) is solved with a fairly low accuracy. Because of the weak conductivity of the human body the term $\widetilde{\mathbf{C}}\mathbf{M}_\nu\mathbf{C}$ converges much faster than the rest of the curl–curl equation, so this step provides an approximate vector potential $\widehat{\mathbf{a}}_{\mathrm{app}}$ that already describes the

magnetic field distribution very well, but does yet not satisfy the quasistatic continuity equation $\widetilde{\mathbf{S}}\mathbf{M}_\kappa\underline{\widehat{\mathbf{a}}}_{\mathrm{app}} = 0$. Using the same decomposition as in (7) yields

$$\underline{\widehat{\mathbf{a}}} = \underline{\widehat{\mathbf{a}}}_{\mathrm{app}} - \widetilde{\mathbf{S}}^{\mathrm{T}}\underline{\phi}_{\mathrm{corr}}. \tag{11}$$

Because in the exact solution $\widetilde{\mathbf{S}}\mathbf{M}_\kappa\underline{\widehat{\mathbf{a}}} = 0$ has to be fulfilled, we obtain:

$$\widetilde{\mathbf{S}}\mathbf{M}_\kappa\widetilde{\mathbf{S}}^{\mathrm{T}}\underline{\phi}_{\mathrm{corr}} = \widetilde{\mathbf{S}}\mathbf{M}_\kappa\underline{\widehat{\mathbf{a}}}_{\mathrm{app}} \tag{12}$$

which is the SPFD equation (10), and has to be solved in the second step of the Ex-SPFD approach. It can be understood as a divergence correction applied to the previously calculated magnetic vector potential. The corrected magnetic vector potential $\underline{\widehat{\mathbf{a}}}$ can be calculated with Eq. (11).

At this stage it may seem that the Ex-SPFD approach is more complicated than simply solving the curl–curl equation of Section 3.2. But this is not true when analyzing the convergence behavior of the schemes. Due to the low conductivity values of biological tissue a very high accuracy is needed when solving the full electromagnetic curl–curl equation in order to obtain reliable values for the induced currents, resulting in very large computation time. Using the two-step procedure of the Ex-SPFD approach the computational time is reduced considerably (see Section 4 for computation times). Furthermore, additional flexibility is introduced in the computational scheme: Each calculation step can be performed on a different grid. In the first step, a vector-based quantity is computed, demanding three degrees of freedom per grid cell, while in the second step a scalar equation is solved, needing only one degree of freedom per grid cell. Using less core memory, this allows in practice to choose a finer resolution for the second calculation step. This option has also been implemented, using a grid transfer operator $\mathbf{P}^h_{L,H}$, prolongating the magnetic vector potential from the coarse grid G_H, on which in the electromagnetic curl–curl equation is solved, to a fine grid G_h on which the divergence correction is applied. For the construction of this operator, see Appendix A.

Algorithm 1. Ex-SPFD scheme

1. Solve

$$[\widetilde{\mathbf{C}}_H\mathbf{M}_{v,H}\mathbf{C}_H + \mathbf{M}_{\kappa,H}\widetilde{\mathbf{S}}_H^{\mathrm{T}}\mathbf{M}_{N,H}\widetilde{\mathbf{S}}_H\mathbf{M}_{\kappa,H} + \mathrm{i}\omega\mathbf{M}_{\kappa,H}]\underline{\widehat{\mathbf{e}}}_H = -\mathrm{i}\omega\underline{\widehat{\mathbf{j}}}_{s,H} \tag{13}$$

   on a coarse grid G_H with a relatively low solver tolerance, obtaining $\underline{\widehat{\mathbf{a}}}_H = -\frac{1}{\mathrm{i}\omega}\underline{\widehat{\mathbf{e}}}_H$
2. (optional) Prolongate the magnetic vector potential from the coarse to the fine grid: $\widehat{\mathbf{a}}_h = \mathbf{P}^h_{L,H}\widehat{\mathbf{a}}_H$
3. Solve the divergence correction

$$\widetilde{\mathbf{S}}_h\mathbf{M}_{\kappa,h}\widetilde{\mathbf{S}}_h^{\mathrm{T}}\underline{\phi}_h = -\widetilde{\mathbf{S}}_h\mathbf{M}_{\kappa,h}\mathbf{P}^h_{L,H}\underline{\widehat{\mathbf{a}}}_H \tag{14}$$

   on the fine grid G_h
4. Apply correction to the prolongated vector potential:

$$\underline{\widehat{\mathbf{a}}}_h = \mathbf{P}^h_{L,H}\widehat{\mathbf{a}}_H - \widetilde{\mathbf{S}}_h\underline{\phi}_h. \tag{15}$$

5. Calculate the induced currents by:

$$\underline{\widehat{\mathbf{j}}}_{\mathrm{induced},h} = -\mathrm{i}\omega\mathbf{M}_{\kappa,h}\underline{\widehat{\mathbf{a}}}_h. \tag{16}$$

Numerical experiments proved that in the solution of the electromagnetic curl–curl equation the contribution to the current density inside the body originating from displacement currents is negligible. Furthermore, the displacement currents are not explicitly considered in the SPFD approach. Therefore, in the first step of the Ex-SPFD approach the full electromagnetic curl–curl equation will be solved omitting the permittivity.

With this scheme it is possible to calculate currents induced by arbitrarily shaped magnetic field sources at a far lower computational time, than by simply solving the full electromagnetic curl–curl equation (6). Furthermore, highly conductive materials that shield the magnetic field are allowed in the computational domain, which is an additive advantage over the classical SPFD approach. A direct comparison of all computational times and errors of the presented approaches will be given in Section 4.

4. Numerical results

At the beginning of this section a test case used for a performance test of the presented formulations is introduced, followed by results in the case of equal coarse and fine grid. These results are followed by a convergence study in the case where the coarse grid solution is prolongated onto a finer grid, before applying the second step of the Ex-SPFD approach. Finally, this section ends with some remarks on the implementation of the Ex-SPFD code.

4.1. Test case

The test case for the performance study of the presented codes is illustrated in Fig. 1. It consists of the upper part of the human-body model, approximately starting at the hips. In the right shoulder, a small block of a highly conductive material (conductivity = 1e6 S/m) can be inserted, representing e.g. a metallic implant. In this example, it is used to demonstrate the validity of the Ex-SPFD approach, even when highly conductive objects are situated inside the computational domain. The magnetic field is excited by a circular current path in front of the chest of the model. The current inside this coil model amounts to 5 A. The model is meshed with 327,026 grid cells in the case without the conductive block (case (a)), and 329,280 cells in the case with the block (case (b)). This number of grid cells corresponds to an approximate resolution of 8 mm. The reference solutions for all further comparisons in this paper are results for the presented models obtained by the curl–curl equation (6) at the maximal feasible available solver tolerance of $1e-15$. In order to distinguish the fact that the curl–curl equation can be used to solve the entire system in one step and also the curl–curl equation is used in the first step of the (Ex)-SPFD approach we attach a † symbol every time the curl–curl equation is used as the first step of the (Ex)-SPFD approach.

4.2. Equal-grid case

The first numerical experiments presented in this paper discuss the case where the coarse grid and fine grid are identical. In this case, no prolongation of the magnetic vector potential is needed. The results for case (b) are summarized in Table 3, while results for case (a) are presented in Table 2.

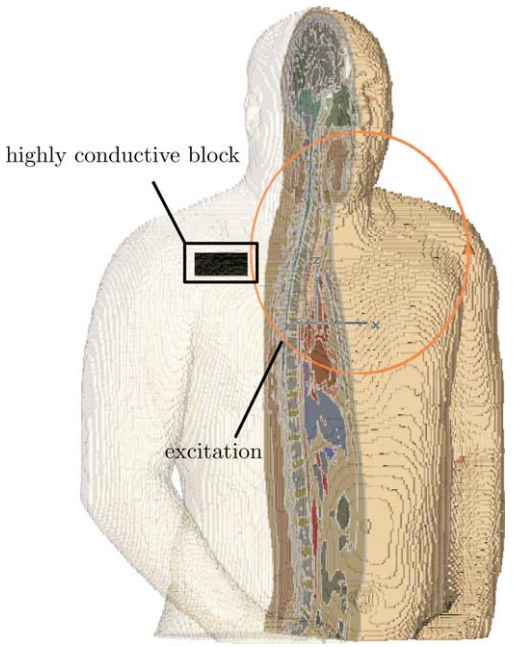

Fig. 1. Test case for validation and numerical performance tests.

Table 2
Simulation results for the test case without the highly conductive block

Solver type	Solver tolerance curl–curl	Solver tolerance divergence correction	Time (hh:mm:ss)	Total time (hh:mm:ss)	Global error (%)
curl–curl (ref)	1e − 15	–	21:46:00	–	–
curl–curl	1e − 9	–	00:12:06	–	56.3
curl–curl	1e − 6	–	00:01:29	–	125.2
SPFD(A)	1e − 6†	1e − 9	00:00:15	00:01:51	3.4e − 3
SPFD(J)	1e − 6†	1e − 9	00:00:47	00:02:23	3.4e − 3
Ex-SPFD(A)	1e − 6†	1e − 9	00:00:30	00:01:59	1.8e − 3
Ex-SPFD(J)	1e − 6†	1e − 9	00:01:34	00:03:03	1.8e − 3
SPFD(A)	1e − 9†	1e − 9	00:00:15	00:02:32	2.0e − 4
SPFD(J)	1e − 9†	1e − 9	00:00:50	00:03:07	2.0e − 4
Ex-SPFD(A)	1e − 9†	1e − 9	00:00:30	00:12:36	2.0e − 4
Ex-SPFD(J)	1e − 9†	1e − 9	00:01:52	00:13:58	2.0e − 4

(A) denotes the FGMRES solver preconditioned by AMG, whereas (J) denotes Jacobi preconditioned CG.

As already pointed out in Section 4.1, the reference solution used for estimation of error values is the solution of the full curl–curl equation, considering the permittivity, with the maximal in double precision feasible solver tolerance of 1e − 15. The global error was computed in the relative power loss norm:

$$\| \widehat{\mathbf{j}} \|_{\text{loss}} = \sqrt{\frac{(\widehat{\mathbf{j}}_{\text{ref}} - \widehat{\mathbf{j}})^{\mathrm{T}} \mathbf{M}_{\kappa^{-1}} \left(\widehat{\mathbf{j}}_{\text{ref}} - \widehat{\mathbf{j}} \right)}{\widehat{\mathbf{j}}_{\text{ref}}^{\mathrm{T}} \mathbf{M}_{\kappa^{-1}} \widehat{\mathbf{j}}_{\text{ref}}}},$$

corresponding to the losses in the tissue. The total time is an addition of the time required to solve the curl–curl† and the SPFD equation, formatted as hh:mm:ss. The letters in brackets denote the solver type used for the divergence correction step: (A) for algebraic multi grid (AMG) preconditioned flexible generalized minimal residual method (FGMRES) and (J) for Jacobi preconditioned conjugate gradient (CG) method. All calculations have been performed on a 3.06 GHz Pentium IV machine with 2 GB RAM.

The time needed to obtain the reference solution amounts to 73 h 21 min in the case where the highly conductive block is present and 21 h 46 min without the block. The very large computational times are due to the chosen maximal solver tolerance of 1e − 15. The need of such a strict solver tolerance arises due to the different orders of magnitude of the $\widetilde{\mathbf{C}}\mathbf{M}_{\nu}\mathbf{C}$ term and the $\mathrm{i}\omega\mathbf{M}_{\kappa} - \omega^2 \mathbf{M}_{\varepsilon}$ term, as stated in Section 3.2. Thus, solving the entire system using only the curl–curl is possible but due to the high computational times not practicable. Since the curl–curl equation does not include any approximations and thus represents a solution of the full Maxwell equations it will be used as the reference solution. The difference in the solution times for both cases can be explained by a severe deterioration of the condition number of the system matrix by introducing the highly conductive block.

In the following we compare the reference solution to three cases:

- A solution of the curl–curl equation with a less strict solver tolerance and without applying a divergence correction.
- The SPFD approach.
- The Ex-SPFD approach.

A solution of the curl–curl equation with a less strict solver tolerance and without applying a divergence correction. The errors of the curl–curl solutions obtained with a less strict solver tolerance (1e − 9 and 1e − 6) are far larger in the case without the block than in the case containing the block (56.3% and 125.2% versus 0.8% and 5.1%). This can be explained by the very large currents induced inside and at the surface of the block, obscuring the details of the solution inside the low-conductive body, even when using a weighted error norm like the power loss norm. These calculated errors demonstrate the need of the very low solver tolerance when solving the whole system with only the curl–curl equation.

The SPFD approach. In the simulation using the SPFD formulation the magnetic vector potential was also computed by the curl–curl† equation but with all conductivities in the curl–curl† equation set to zero, corresponding to a neglect of the shielding effects introduced by the highly conductive block. For the case without the block the SPFD approach performs very well, exhibiting a global error of 3.4e − 3% when the curl–curl† equation in the first step is solved with an accuracy of 1e − 6, and a global error of 2.0e − 4% when the curl–curl† equation was solved with an accuracy of 1e − 9. When the conductive block is present the error of this approach rises about three orders magnitude to 1.9% because the shielding effects are neglected in the computation of the magnetic vector potential. As expected, an more strict solver tolerance in the curl–curl† solution has no effect on the errors. The computational time remains below 3:30 min in both cases.

The Ex-SPFD approach. The results of the full Ex-SPFD approach (without prolongation, since we deal with equal grids in this paragraph) exhibit the lowest errors in all presented cases. In the case when no conductive block is present the estimated errors are similar to the SPFD approach, but the computational time is slightly raised: At a solver tolerance of 1e − 9 in the solution of the curl–curl† equation the global error of both approaches amounts to 2.0e − 4% but the computational time is raised to approximately 14 min for Ex-SPFD. On the other hand, in the case containing the higly conductive block the global error of the Ex-SPFD approach remains low at 2.2e − 3% or 2.2e − 5% for a curl–curl† solution with a solver tolerance of 1e − 6 and 1e − 9, respectively. Because we have considered the conductivity in the computation of the magnetic vector potential, the shielding effects were considered, resulting in a more exact solution than in the SPFD approach. When the curl–curl† equation is solved with a tolerance of 1e − 6 the time for the entire Ex-SPFD computation amounts to 5:26 min.

For both approaches the divergence correction steps were performed using AMG preconditioned FGMRES and Jacobi preconditioned CG. This is indicated by letters in brackets in Tables 2 and 3. In the case containing no block the computational time of the AMG-FGMRES solver is smaller by a factor of three compared to Jacobi-CG. The acceleration of the computation using the AMG-FGMRES raises to a factor of six in the model containing the highly conductive block, illustrating the superior performance of the AMG preconditioning for badly conditioned matrices. Furthermore, multigrid preconditioning exhibits an ideal asymptotic complexity. Therefore, it is the state-of-the art choice for large ill-conditioned systems of equations.

From the data presented in Tables 2 and 3 the superior performance of the Ex-SPFD code can be concluded. This approach drastically lowers the computation time compared to a solution using only the curl–curl equation and is, in contrast to the SPFD approach, also valid when highly conductive materials have to be considered in the computational domain. Furthermore, the calculation of the magnetic vector potential using the curl–curl† equation allows arbitrarily shaped magnetic field sources contrary to the classical SPFD approach, which is restricted to analytical and semi-analytical sources. The so far presented results cover only the case of equal grids in the two stages of the Ex-SPFD approach. The Ex-SPFD approach however also allows the usage of two grids with a different resolution. In the next subsection a convergence study in the case of non-equal grids will be presented.

Table 3
Simulation results for the test case containing the highly conductive block

Solver type	Solver tolerance curl–curl	Solver tolerance divergence correction	Time (hh:mm:ss)	Total time (hh:mm:ss)	Global error (%)
curl–curl (ref)	1e − 15	–	73:21:00	–	–
curl–curl	1e − 9	–	01:41:59	–	0.8
curl–curl	1e − 6	–	00:03:23	–	5.1
SPFD(A)	1e − 6†	1e − 9	00:00:10	00:01:38	1.9
SPFD(J)	1e − 6†	1e − 9	00:00:58	00:02:26	1.9
Ex-SPFD(A)	1e − 6†	1e − 9	00:00:23	00:03:46	2.2e − 3
Ex-SPFD(J)	1e − 6†	1e − 9	00:02:03	00:05:26	2.2e − 3
SPFD(A)	1e − 9†	1e − 9	00:00:10	00:02:26	1.9
SPFD(J)	1e − 9†	1e − 9	00:01:03	00:03:19	1.9
Ex-SPFD(A)	1e − 9†	1e − 9	00:00:26	01:42:25	2.2e − 5
Ex-SPFD(J)	1e − 9†	1e − 9	00:01:52	01:43:51	2.2e − 5

(A) denotes the FGMRES solver preconditioned by AMG, whereas (J) denotes Jacobi preconditioned CG.

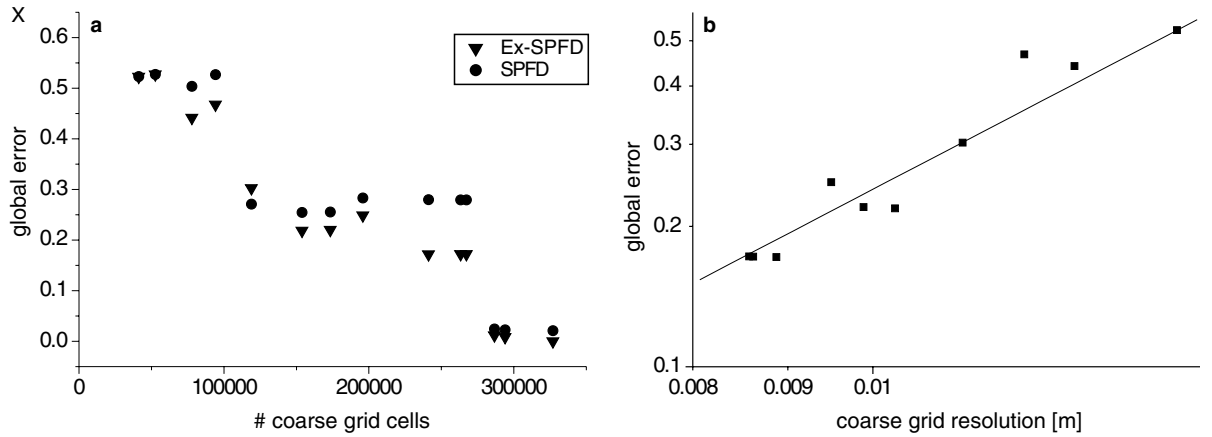

Fig. 2. (a) The global error versus the number of coarse grid cells for the test case containing the highly conductive block. Ex-SPFD results are denoted as triangles, SPFD results as circles. (b) The global error plotted versus the coarse grid resolution and a linear least-squares fit of the data.

4.3. Non-equal grids case

In this subsection, the performance of the Ex-SPFD formulation in the case of non-equal grids for the two stages of the approach is presented. In this case, the vector-based curl–curl equation is solved on a coarse grid, the vector potential is then prolongated onto a finer grid, where the SPFD equation is applied. The prolongation is performed using trilinear interpolation, as described in Appendix A. The used reference solution is a fine grid curl–curl solution with an solver tolerance of $1e-15$, which is the same as in previous section.

The global error in relation to the number of coarse grid cells for the test case containing the highly conductive block is depicted in Fig. 2(a). The results of the Ex-SPFD approach are denoted by triangles, the SPFD results by circles. The Ex-SPFD formulation achieves a smaller error for all but one coarse grid resolution (119000 coarse grid cells) which is in accordance with the results for the equal-grid case. Due to the used meshing algorithm, the error exhibits a step-like increase when reducing the number of coarse grid cells: The voxel data is re-meshed for every resolution using an averaging algorithm over four primal facets, resulting in a step-like increase of the error at certain resolutions where details of the model are no longer considered due to the coarser resolution. Using a more sophisticated averaging algorithm for the material distribution like the Galerkin projection [35] would allow to overcome this behavior, but it also would lead to non-diagonal material matrices, and has not been implemented here. Using a double logarithmic plot of the global error versus the grid resolution (Fig. 2(b)) the order of convergence can be estimated. The linear least-squares fit of the data exhibits a slope of approximately 2, hence the Ex-SPFD approach is second order convergent with respect to the coarse grid resolution.

The results presented in this subsection illustrate the performance of the Ex-SPFD approach in the case when the curl–curl solution is prolongated before the second step of the Ex-SPFD scheme. This second step has been implemented in a parallel environment, in order to distribute the system to be solved onto multiple computers and handle finer resolutions.

4.4. Implementation issues

For the curl–curl solver used in this article, as well as for the meshing routines, commercially available software is used.[1] The maximum possible number of grid cells for the curl–curl solver amounts to approximately 1.5 millions when 2 GB of RAM are available, which is the limit for MS-Windows based 32-Bit architecture PC's. The used meshing routines can handle problems up to approximately 9.4 million grid cells on the same platform. The solver for the divergence correction in the second step of the Ex-SPFD approach has been

[1] CST EM-Studio 1.3, www.cst.com.

implemented in a parallel environment using the portable, extensible toolkit for scientific computation (PETSc) [36]. The algebraic multigrid preconditioning is done by BoomerAMG included in the Hypre package [37]. The main reason for the parallel implementation is the large memory demand of the finely resolved models. Because the system matrix in the second step of the Ex-SPFD approach only consists of real-valued coefficients, it is possible to solve the real and imaginary part of the system separately. The successive solution of the system is less memory-intensive.

The AMG preconditioner accelerates the solution process for the test case by a factor of approximately five, but it also exhibits a substantially larger memory demand. Using eight double processor cluster PC's, all equipped with 2 GB core memory, the largest problem solvable with the available AMG preconditioning software consists of 5.5 million cells. The same problem can be solved with Jacobi CG on three such PCs. Hence, to circumvent the memory restriction, the fine resolved examples presented in the next section are solved using Jacobi CG.

5. Application example

After demonstrating the validity and the improved performance of the Ex-SPFD approach in the previous section, a realistic application example for the new code will be introduced in this section. We simulate the currents induced by an electric blanket considering two different wiring configurations. The two different wiring configuration are depicted in Fig. 3. Electric blankets are quite widely spread throughout households and typically cover nearly the entire body when used, leading to a large exposition area. Simulation results of electric blankets, computed using the impedance method can be found in [38].

In the first configuration, the ends of the heating windings are closed by a straight wire, while in the second configuration the back and forth wires are arranged in parallel. The wiring of the blanket is arranged at a constant distance to the body, therefore the blanket geometry is not planar resulting in a fully three-dimensional field source. The current inside these wires is set to 0.65 A corresponding to 150 W heating power at a voltage of 230 V. With these parameters, the maximal magnetic field strength in close proximity to the wires amounts to 73.7 μT in case (a) and 78.1 μT in case (b). In the first step of the Ex-SPFD approach, the curl–curl equation was solved up to a solver tolerance of $1e-6$ on a coarse grid consisting of about 1.5 million cells (6.2 mm). For the second step, both models were meshed with approximately 9.3 million grid cells, corresponding to a mean spatial resolution of 3.4 mm. The divergence correction is applied using 6 PC's ($12\times$ Intel Xeon 3 GHz, 2 GB RAM) in parallel. This simulation took 35 min for a solver tolerance of $1e-9$ using Jacobi CG.

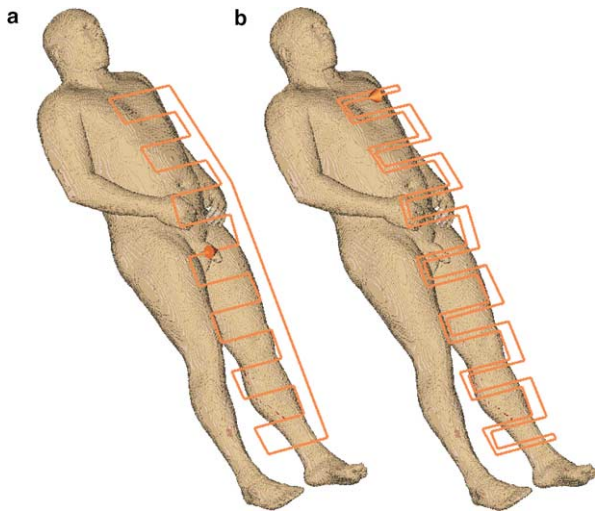

Fig. 3. Two simulated wiring configurations of an electric blanket.

Table 4
Organ-wise induced current densities originating from an electric blanket

Tissue type	Induced current density (A/m^2)			
	Case (a)		Case (b)	
	Mean	Max	Mean	Max
Whole body	7.02e − 7	1.03e − 5	3.13e − 7	4.38e − 6
Marrow	5.44e − 8	7.89e − 6	2.54e − 8	3.43e − 6
Fat tissue	1.96e − 7	6.79e − 6	9.11e − 8	2.72e − 6
Bones	1.41e − 7	9.04e − 6	6.85e − 8	3.85e − 6
White substance	1.54e − 7	7.94e − 7	7.89e − 8	4.07e − 7
Grey substance	1.84e − 7	1.19e − 6	9.41e − 8	6.11e − 7
Skin	3.83e − 7	1.62e − 6	1.87e − 7	8.06e − 7
Eye	4.22e − 7	8.86e − 7	2.15e − 7	4.53e − 7
Skeleton muscle	6.98e − 7	1.03e − 5	3.42e − 7	4.38e − 6
Blood	1.13e − 6	5.58e − 6	5.11e − 7	2.64e − 6
Neuronal fabric	7.44e − 8	1.16e − 6	3.78e − 8	5.93e − 7
Nervus opticus	9.22e − 8	1.16e − 6	4.67e − 8	5.94e − 7
Cartilages	7.61e − 7	5.11e − 6	3.17e − 7	2.20e − 6
Mucous membrane	7.09e − 9	3.33e − 7	3.64e − 9	1.74e − 7
Lung	6.09e − 7	3.88e − 6	2.63e − 7	1.69e − 6
Intestine	1.63e − 6	7.91e − 6	6.01e − 7	3.14e − 6
Kidney	3.31e − 7	2.01e − 6	1.45e − 7	8.19e − 7
Liver	3.12e − 7	5.06e − 6	1.36e − 7	2.23e − 6
Glands	9.47e − 7	4.64e − 6	4.67e − 7	2.13e − 6
Spleen	3.25e − 7	1.14e − 6	1.55e − 7	5.39e − 7
Stomach	8.12e − 7	6.78e − 6	4.17e − 7	2.46e − 6
Pancreas	1.08e − 6	2.57e − 6	4.58e − 7	1.13e − 6
Bladder	4.34e − 7	1.18e − 6	2.06e − 7	6.39e − 7
Gall bladder	1.83e − 6	6.28e − 6	8.13e − 7	2.77e − 6
Intestine contents	1.88e − 6	9.26e − 6	7.60e − 7	3.65e − 6
Ventricles right	6.10e − 7	4.06e − 6	2.89e − 7	1.70e − 6
Ventricles left	4.70e − 7	2.59e − 6	2.32e − 7	1.11e − 6
Forecourt right	9.56e − 7	3.50e − 6	4.23e − 7	1.46e − 6
Forecourt left	8.34e − 7	2.52e − 6	3.70e − 7	1.11e − 6
Blood venous	1.71e − 6	6.48e − 6	7.70e − 7	2.86e − 6
Blood arterial	2.00e − 6	4.77e − 6	8.74e − 7	2.03e − 6

The used wiring configurations are depicted in Fig. 3.

The organ-wise evaluated results of the simulations are summarized in Table 4. The maximum induced current density inside the whole body amounts to 1.03e − 5 A/m^2 for case (a) and 4.38e − 6 A/m^2 for case (b). Both values are situated well below the *ICNIRP* restriction for the general public (2e − 3 A/m^2). The value of 1e − 5 A/m^2 is only surpassed in case (a) for skeleton muscle, all other current densities are below this level. Generally, nearly all induced current densities in case (b) are smaller by a factor of two compared to case (a), even though the maximal magnetic field intensity is lower in case (a). This effect is mainly due to the reduced area enclosed by the current paths in case (b), and demonstrates the necessity of a geometrically realistic modeling of the field sources in calculations of induced current densities inside the human body. Plots of the induced current densities in the coronal and midsagittal plane for both wiring configurations are depicted in Fig. 4. The used color ramp can be found beneath the plots. Black represents areas of lowest current densities, while white domains stand for the maximal current densities of 5 mA/m^2. This plot demonstrates the results of Table 4 graphically: the induced current densities in case (b) are lower by a factor of two than in case (a).

6. Summary

In this work, we have presented a new approach for the computation of induced current densities in anatomically realistic, high-resolution human-body models. The proposed Ex-SPFD approach allows a

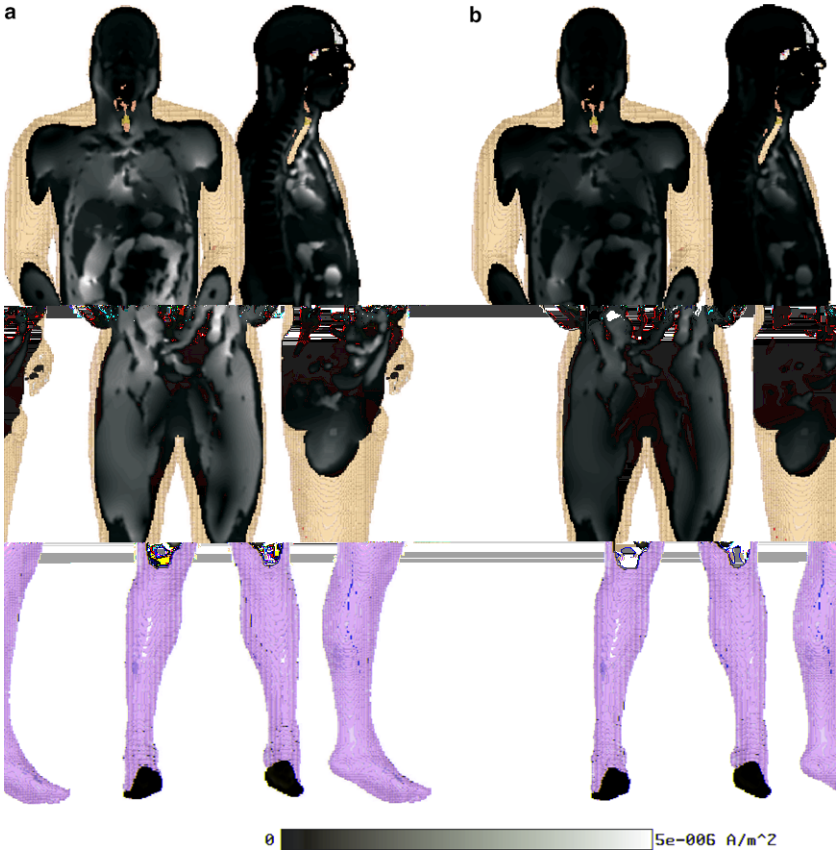

Fig. 4. Plot of the induced current densities in the coronal and midsagittal plane for both wiring configurations. The color codes used are depicted in the color ramp beneath the plots. (For interpretation of the references to color in this figure legend, the reader is referred to the web version of this article.)

very efficient computation by applying a two-step procedure using a combination of the curl–curl equation and the classical SPFD approach. The newly developed scheme is superior to the curl–curl formulation in terms of computation time, and allows to handle arbitrarily shaped magnetic field sources. Furthermore, shielding effects of highly conductive material on the external magnetic field are explicitly considered thus, clearly extending the SPFD approach. Using two different grids for both steps of the Ex-SPFD approach allows to choose a very fine resolution, since the second step has been implemented in a parallel environment. The drastic reduction of computational time was confirmed by the numerical experiments presented in Section 4 using two different test cases. Finally, a realistic exposure situation was presented in Section 5. The results of these simulations of an electric blanked with two wiring configurations, discretized with approximately 9.3 million grid cells, indicated the need for a geometrically realistic modeling of the field sources. Although the maximal magnetic flux in wiring case (b) was somehow higher than in case (a), the induced current densities were reduced by a factor of two in case (b) due to the geometric shape of the heating wires.

Acknowledgments

A. Barchanski is supported by the Deutsche Forschungsgemeinschaft (DFG) under grants WE1239/19-1. H. De Gersem is working in the cooperation project DA-WE1 (TEMF/GSI) with the Gesellschaft für Schwerionenforschung (GSI), Darmstadt.

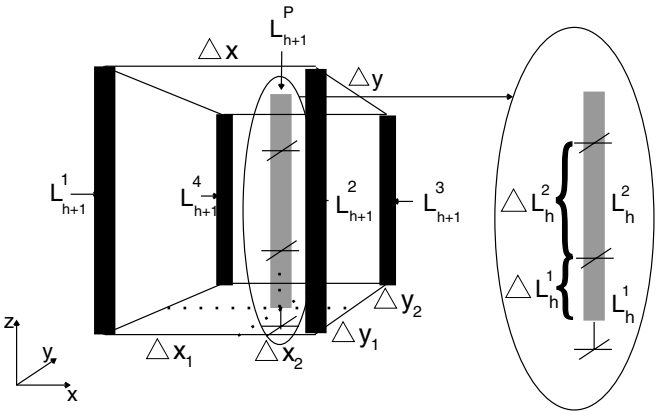

Fig. 5. Prolonagation of integral state quantities allocated on edges.

Appendix A. Prolongation of edge-based quantities

Since the grids in both steps of the Ex-SPFD approach are non-nested, an interpolation operator is required to prolongate the magnetic vector potential from the initial coarse grid to the fine grid used for the divergence correction. The prolongation is performed using trilinear interpolation, as sketched in Fig. 5. The four closest edge quantities of the coarse grid are projected on the edges of the fine grid, e.g., for a component in the z-direction:

$$\widehat{\mathbf{L}}^{P}_{h+1} = w^{y}_{1} w^{x}_{1} \widehat{\mathbf{L}}^{1}_{h+1} + w^{y}_{1} w^{x}_{2} \widehat{\mathbf{L}}^{2}_{h+1} + w^{y}_{2} w^{x}_{1} \widehat{\mathbf{L}}^{3}_{h+1} + w^{y}_{2} w^{x}_{2} \widehat{\mathbf{L}}^{4}_{h+1},$$

with the factors

$$w^{x}_{i} = \frac{\Delta x - \Delta x_i}{\Delta x} \quad \text{and} \quad w^{y}_{i} = \frac{\Delta y - \Delta y_i}{\Delta y}.$$

In the next step the projected quantity $\widehat{\mathbf{L}}^{P}_{h+1}$ is divided according to the lengths of the edges of the fine grid L^{j}_{h} overlapping with L^{P}_{h+1}

$$\widehat{\mathbf{L}}^{j}_{h} = \sum_{L^{P}_{h+1}\ \text{overlapping}\ L^{j}_{h}} w^{z}_{j} \widehat{\mathbf{L}}^{P}_{h+1},$$

where $w^{z}_{j} = \frac{\Delta L^{j}_{h}}{|L^{P}_{h+1}|}$.

This scheme is a part of the geometric multigrid algorithm for use with the conformal FIT published in [35].

References

[1] Strahlenschutzkommission, Grenzwerte und Vorsorgenaßnahmen zum Schutz der Bevölkerung vor elektromagnetischen Feldern, Technical Report, Strahlenschutzkomission, 2001 (in German).
[2] ICNRIP, Guidelines for limiting exposure to time-varying electric, magnetic, and electromagnetic fields (up to 300 GHz), Technical Report, ICNIRP, 2001.
[3] O.P. Gandhi, J.F. Deford, H. Kanai, Impedance method for calculation of power deposition patterns in magnetically induced hyperthermia, IEEE Trans. Biomed. Eng. 31 (10) (1984) 644–651.
[4] N. Orcutt, O.P. Gandhi, A 3-D impedance method to calculate power deposition in biological material subjected to time varying magnetic fields, IEEE Trans. Biomed. Eng. 35 (8) (1988) 577–583.
[5] O.P. Gandhi, J-Y. Chen, Numerical dosimetry at power-line frequencies using anatomically based models, IEEE Trans. Biomed. Eng. (Suppl. 1) (1992) 43–60.
[6] W.G. Xi, M.A. Stuchly, O.P. Gandhi, Induced electric currents in models of man and rodents from 60-Hz magnetic-fields, IEEE Trans. Biomed. Eng. 41 (11) (1994) 1018–1024.
[7] Trevor W. Dawson, Maria A. Stuchly, Analytic validation of a three-dimensional scalar-potential finite-difference code for low-frequency magnetic induction, ACES J. 11 (3) (1996) 72–81.

[8] Trevor W. Dawson, Jan de Moerloose, Maria A. Stuchly, Comparison of magnetically induced ELF fields in humans computed by FDTD and scalar potential FD codes, ACES J. 11 (3) (1996) 63–71.
[9] Trevor W. Dawson, Kris Caputa, Maria A. Stuchly, A comparison of 60 Hz uniform magnetic and electric induction in the human body, Phys. Med. Biol. 42 (1997) 2319–2329.
[10] M.A. Stuchly, O.P. Gandhi, Inter-laboratory comparison of numerical dosimetry for human exposure to 60 Hz electric and magnetic fields, Bioelectromagnetics 21 (2000) 167–174.
[11] Trevor W. Dawson, Maria A. Stuchly, Interaction of low-frequency electric and magnetic fields with the human body, Proc. IEEE 88 (5) (2000) 643–666.
[12] C.C. Johnson, C.H. Durney, H. Massoudi, Long-wavelength electromagnetic power absorption in prolate spheroidal models of man and animals, IEEE Trans. Microwave Theory Tech. 23 (1975) 739.
[13] C.H. Durney, M.F. Iskander, H. Massoudi, C.C. Johnson, An empirical formula for broadband SAR calculations of prolate spheroidal models of humans and animals, IEEE Trans. Microwave Theory Tech. 27 (1979) 758.
[14] M.J. Hagman, O.P. Gandhi, C.H. Durney, Numerical calculation of electromagnetic energy deposition for a realistic model of man, IEEE Trans. Microwave Theory Tech. 27 (1979) 804.
[15] V. Spitzer, M.J. Ackerman, A.L. Scherzinger, D. Whitlock, The visible human male: A technical report, J. Am. Med. Inform. Assoc. 3 (1996) 118–130.
[16] Ecole Polytechnique Fédérale de Lausanne. Available from: <http://visiblehuman.epfl.ch>.
[17] P.J. Dimbylow, Current densities in a 2 mm resolution anatomically realistic model of the body induced by low frequency electric fields, Phys. Med. Biol. 45 (2000) 1013–1022.
[18] O.P. Gandhi, Gang Kang, Ding Wu, Gianluca Lazzi, Currents induced in anatomic models of the human for uniform and nonuniform power frequency magnetic fields, Bioelectromagnetics 22 (2001) 112–121.
[19] Watanabe et al., Development of voxel male and female whole body models and dosimetry, in: Proceedings of the URSI 2002 Conference, Maastricht, The Netherlands, August, 2002.
[20] Kenneth S. Cole, Membranes, Ions and Impulses, University of California Press, Berkeley, Los Angeles, London, 1972.
[21] S. Gabriel, E. Corthout, C. Gabriel, The dielectric properties of biological tissues: I. Literature survey, Phys. Med. Biol. 41 (1996) 2231–2249.
[22] S. Gabriel, R.W. Lau, C. Gabriel, The dielectric properties of biological tissues: II. Measurements in the frequency range 10 Hz to 20 GHz, Phys. Med. Biol. 41 (1996) 2251–2269.
[23] S. Gabriel, R.W. Lau, C. Gabriel, The dielectric properties of biological tissues: III. Parametric models for the dielectric spectrum of tissues, Phys. Med. Biol. 41 (1996) 2271–2293.
[24] Thomas Weiland, A discretization method for the solution of Maxwell's equations for six-component fields, Electron. Commun. AEÜ 31 (3) (1977) 116–120.
[25] T. Weiland, Time domain electromagnetic field computation with finite difference methods, Int. J. Numer. Mod.: ENDF 9 (1996) 259–319.
[26] M. Bartsch, U. Becker, M. Dehler, M. Dohlus, Xingjun Du, S. Gutschling, R. Klatt, F. Krawczyk, M. Marx, M. Zhang, T. Pröpper, D. Schmitt, P. Schntt, B. Steffen, P. Thoma, B. Wagner, T. Weiland, S.G. Wipf, H. Wolter, Finite integration: Ein universell anwendbares Verfahren zur Berechnung elektromagnetischer Felder, in: VDE- Fachberichte 45, Biologische Wirkungen elektromagnetischer Felder (VortrSge der VDE Fachtagung in Bad Nauheim, 9–10 November 1993), 1993. pp. 109–118.
[27] T. Weiland, R. Schumann, Discrete electromagnetism by the finite integration technique, J. Jpn. Soc. Appl. Electromagn. Mech. 10 (2) (2002) 159–169.
[28] M. Clemens, Large systems of equations in discrete electromagnetism: formulations and numerical algorithms, IEE Proc. Sci. Meas. Technol. 152 (2) (2005) 50–72.
[29] Thomas Weiland, Time domain electromagnetic field computation with finite difference methods, Int. J. Numer. Modelling 9 (1996) 259–319.
[30] Thomas Weiland, Lossy waveguides with arbitrary boundary contour and distribution of material, Electron. Commun. AEÜ 33 (1979) 170.
[31] M. Clemens, T. Weiland, M. Wilke, Transient eddy current formulation including moving conductors using the FI method, IEEE Trans. Magn. 4 (1) (2002) 804–808.
[32] B. Krietenstein, P. Thoma, R. Schuhmann, T. Weiland, Facing the big challenge of high precision field computation, in: Proceedings of the 19th LINAC Conference, Chicago, August, 1998.
[33] P. Hahne, T. Weiland, 3D Eddy current computation in the frequency domain regarding the displacement current, IEEE Trans. Magn. 28 (2) (1992) 1801–1804.
[34] M. Clemens, T. Weiland, Regularization of eddy current formulations using discrete grad–div operators, IEEE Trans. Magn. 38 (2) (2002) 569–572.
[35] S. Feigh, M. Clemens, T. Weiland, Geometric multigrid method for electro- and magnetostatic field simulations using the conformal finite integration technique, Numer. Lin. Algebra Appl. (2003).
[36] S. Balay, V. Eijkhout, W.D. Gropp, L.C. McInnes, B.F. Smith, Modern Software Tools in Scientific Computing, Birkhäuser, Basel, 1997.
[37] V.E. Henson, U.M. Yang, Boomeramg: a parallel algebraic multigrid solver and preconditioner, Appl. Numer. Math. 41 (2002) 155–177.
[38] Om P. Gandhi, Some numerical methods for dosimetry: extremely low frequencies to microwave frequencies, Radio Sci. 30 (1) (1995) 161–177.